ChemComm

COMMUNICATION

View Article Online
View Journal | View Issue

Cite this: *Chem. Commun.*, 2025, **61**, 901

Received 25th September 2024,
Accepted 19th November 2024

DOI: 10.1039/d4cc04970e

rsc.li/chemcomm

Designing Cu–CoO heterostructure nanosheets for efficient electrooxidation of 5-hydroxymethylfurfural to 2,5-furandicarboxylic acid†

Dongfang Ji,[a] Wenke Wang,[a] Ting Sang,[a] Jingcheng Hao,[a] Xiaoyu Zhang*[b] and Zhonghao Li*[a]

We report the design of Cu–CoO heterostructure nanosheets as a highly efficient electrocatalyst for the electrochemical conversion of 5-hydroxymethylfurfural (HMF) to 2,5-furandicarboxylic acid (FDCA). The Cu–CoO nanosheets exhibited remarkable catalytic performance, achieving 100% HMF conversion, 98.2% FDCA yield, and 98.1% Faraday efficiency.

The rapid depletion of fossil fuel reserves has driven the search for alternative and sustainable energy sources.[1] Biomass presents numerous advantages such as low cost and environmental sustainability, making it a prime candidate for substituting fossil fuels in the production of high-value chemicals.[2–4] Among these, 5-hydroxymethylfurfural (HMF), derived from lignocellulosic biomass, stands out as a top 12 biomass derivative and serves as a versatile platform molecule for synthesizing valuable carbon-based products.[5] Its oxidation product, 2,5-furandicarboxylic acid (FDCA), is a critical precursor for bio-based plastics like polyethylene furanoate (PEF), offering an eco-friendly alternative to conventional petroleum-based polyethylene terephthalate (PET).[6,7] Therefore, developing efficient catalysts for HMF conversion to FDCA has become a key focus in biomass conversion research.

In HMF conversion, the electrochemical oxidation approach offers significant advantages, including milder reaction conditions, enhanced safety, and improved environmental sustainability.[8–12] Recently, transition metal electrocatalysts have emerged as attractive candidates for HMF oxidation, with cobalt-based materials receiving particular attention for their electrocatalytic potential.[6,13] However, the activity of cobalt-based electrocatalysts is significantly limited by the oxygen evolution reaction (OER), a competing side reaction that diminishes their overall effectiveness for HMF oxidation. In contrast, copper-based materials show minimal activity towards the OER, reducing competition and making them more promising for selective HMF electrooxidation.[9,14–17] Given this, we propose that the integration of cobalt-based materials with copper-based materials could create a high-efficiency electrocatalyst for HMF conversion, leveraging the advantages of both types of electrocatalysts. This synergistic combination may optimize electrocatalytic performance by improving selectivity and minimizing competing reactions.

Interfacial engineering enables precise control of the electronic environment at material interfaces, improving electrocatalyst design.[18–21] By selectively constructing heterostructures, the combined properties of different components create synergistic effects, enabling improved overall electrocatalytical efficiency.[22] Thus, we hypothesize that a heterostructured catalyst integrating cobalt-based and copper-based materials could be highly effective for HMF conversion.

Building on the above, Cu–CoO heterostructure nanosheets were designed as the electrocatalysts for the electrooxidation of HMF to FDCA. These nanosheets were synthesized using a microwave-assisted deep eutectic solvent (DES) method, followed by pyrolysis. The electrocatalyst demonstrated excellent electroactivity, achieving 100% HMF conversion, 98.2% FDCA yield and 98.1% Faraday efficiency (FE). The enhanced electrooxidation was elucidated by density functional theory (DFT) calculations. This study presents a promising strategy for designing a Cu/Co-based heterostructured electrocatalyst toward high-efficiency electrooxidation of HMF to FDCA.

The Cu–CoO heterostructure nanosheets were fabricated through a microwave-assisted DES method, followed by pyrolysis (Fig. S1, ESI†). The microwave heating of a choline chloride/oxalic acid (ChCl/OA) deep eutectic solvent (DES) containing Co/Cu salts for 10 s resulted in sheet-like Cu/Co-based precursors, as confirmed by transmission electron microscopy (TEM) images (Fig. S2, ESI†). We also performed the precursor synthesis with microwave heating for 15 and 20 s. However, the resultant precursors do not show a well-defined sheetlike structure (Fig. S2c and S3, ESI†).

[a] *Key Laboratory of Colloid and Interface Chemistry, Ministry of Education, Shandong University, Jinan, 250100, China. E-mail: zhonghaoli@sdu.edu.cn*
[b] *Zhejiang Carbon Neutral Innovation Institute & Moganshan Institute of ZJUT at Deqing, Zhejiang University of Technology, Hangzhou 310014, China. E-mail: zhangxiaoyu@zjut.edu.cn*

† Electronic supplementary information (ESI) available: Experimental section, Fig. S1–S24, and Tables S1–S7. See DOI: https://doi.org/10.1039/d4cc04970e

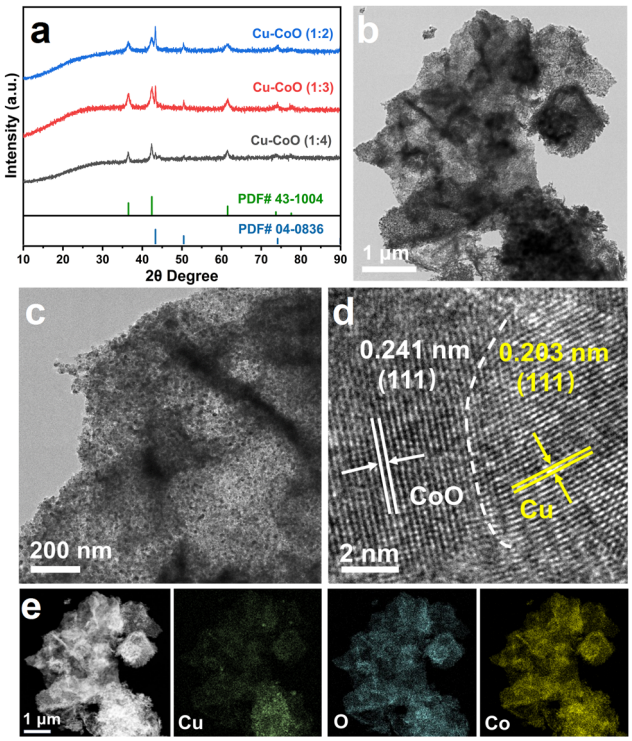

Fig. 1 (a) XRD patterns of Cu–CoO heterostructure nanosheets (1 : 2, 1 : 3, and 1 : 4). (b) and (c) TEM images, (d) HRTEM image, (e) HAADF-STEM image and EDX elemental mapping images of the Cu–CoO heterostructure nanosheets (1 : 3).

Therefore, we selected 10 s as the optimal condition for microwave heating. The obtained precursors were subsequently transformed into Cu–CoO heterostructure nanosheets through pyrolysis. For comparison, Cu–CoO nanosheets with varying Co/Cu atomic ratios were fabricated and labeled as Cu–CoO (x : y), where x : y represents Co/Cu atomic ratio in the initial feed.

Fig. 1a shows the X-ray diffraction (XRD) patterns of the fabricated Cu–CoO with varying Cu/Co atomic ratios. All diffraction peaks align well with those of CoO (PDF# no. 43-1004) and Cu (PDF# no. 04-0836), confirming the successful integration of CoO and Cu in the Cu–CoO products. According to Fig. S4 (ESI†), the diffraction peaks of the cobalt oxide product could be attributed to crystalline CoO (PDF# no. 43-1004). Further characterization was conducted using transmission electron microscopy (TEM) and high-resolution transmission electron microscopy (HRTEM). The TEM images revealed that the Cu–CoO (1 : 3) exhibits a well-defined nanosheet structure (Fig. 1b and c). The HRTEM image distinctly shows the interface between Cu and CoO, with lattice spacings of 0.203 nm and 0.241 nm corresponding to the (111) planes of Cu and (111) planes of CoO, respectively (Fig. 1d). High-angle annular dark-field scanning TEM (HAADF-STEM) and energy-dispersive X-ray (EDX) elemental mapping results demonstrate homogeneous distribution of Co, Cu and O elements in the Cu–CoO (1 : 3) nanosheets (Fig. 1e). Additionally, EDX spectra showed that the atomic ratio of Cu : CoO in Cu–CoO (1 : 2, 1 : 3, and 1 : 4) was 1 : 3.0, 1 : 5.0, and 1 : 7.1, respectively (Fig. S5–S7, ESI†). The morphologies of CoO, Cu–CoO (1 : 2), and Cu–CoO (1 : 4) were also examined, showing a similar nanosheet structure to that of Cu–CoO (1 : 3) (Fig. S8, ESI†).

N_2 adsorption–desorption experiments were performed to evaluate the specific surface areas of the Cu–CoO composites in ratios of 1 : 2, 1 : 3, and 1 : 4, as well as for the pure CoO sample. The Brunauer–Emmett–Teller (BET) specific surface areas of Cu–CoO (1 : 2, 1 : 3, and 1 : 4) and CoO were determined to be 63.6 $m^2\ g^{-1}$, 157.9 $m^2\ g^{-1}$, 108.9 $m^2\ g^{-1}$ and 36.4 $m^2\ g^{-1}$, respectively (Fig. S9, ESI†). The Cu–CoO (1 : 3) sample was further examined using X-ray photoelectron spectroscopy (XPS) (Fig. S10, ESI†). In the Co 2p XPS spectrum (Fig. S10b, ESI†), the characteristic peaks observed at 781.45 eV and 797.75 eV correspond to Co $2p_{3/2}$ and Co $2p_{1/2}$, respectively. Additionally, signals at 786.15 eV and 802.95 eV are ascribed to Co $2p_{3/2}$ and Co $2p_{1/2}$ satellite peaks.[6,23,24] In Fig. S10c (ESI†), a peak centered at 932.60 eV is assigned to Cu $2p_{3/2}$, while another peak around 952.05 eV is owing to Cu $2p_{1/2}$.[15,25,26] Furthermore, in the O 1s XPS spectrum (Fig. S10d, ESI†), signals at 529.75 eV and 531.85 eV correspond to absorbed O and lattice O peaks, respectively.

To assess the HMF electrooxidation performance of the synthesized Cu–CoO heterostructure nanosheets, linear sweep voltammetry (LSV) experiments were conducted, with or without 10 mM HMF. All potentials were referenced to a reversible hydrogen electrode (RHE). This analysis aimed to investigate the electrooxidation capability of the Cu–CoO (1 : 3) nanosheets toward HMF. Upon adding 10 mM HMF to the 1.0 M KOH electrolyte, a significant increase in current density was observed (Fig. 2a), indicating that the HMF electrooxidation is more favorable than the OER. Additionally, the LSV curves of different catalysts (Fig. S11a, ESI†) revealed that Cu–CoO (1 : 3) achieved the highest current density (19.66 mA cm^{-2}, Fig. S12, ESI†) in 10 mM HMF electrolyte at 1.45 V. The superior

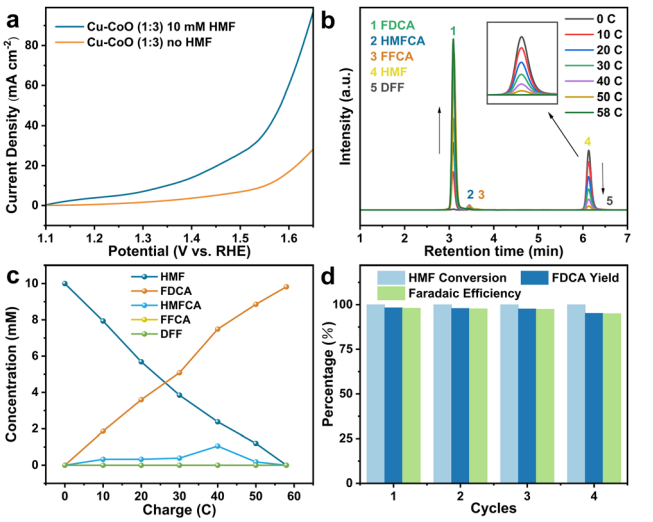

Fig. 2 (a) LSV curves of Cu–CoO (1 : 3) in 1.0 M KOH solution (with or without 10 mM HMF), (b) HPLC chromatogram, (c) concentration change of HMF and oxidation product during the electrooxidation process, and (d) electrooxidation evaluation of HMF for four successive cycles.

electrooxidation activity of Cu–CoO (1 : 3) among the tested catalysts suggests its optimal performance.

Furthermore, compared with CoO (349.5 mV dec^{-1}), Cu–CoO (1 : 2) (318.1 mV dec^{-1}) and Cu–CoO (1 : 4) (323.0 mV dec^{-1}), the Cu–CoO (1 : 3) showed the smallest Tafel slope (280.1 mV dec^{-1}), demonstrating that Cu–CoO (1 : 3) possesses the fastest HMF oxidation reaction kinetics (Fig. S11b, ESI†). Additionally, cyclic voltammetry (CV) was employed to evaluate the electrochemical surface area (ECSA) of the prepared electrocatalysts by determining their double-layer capacitance (C_{dl}) (Fig. S11c and S13, ESI†). The C_{dl} values for CoO, Cu–CoO (1 : 2), Cu–CoO (1 : 3), and Cu–CoO (1 : 4) demonstrated that Cu–CoO (1 : 3) had the highest ECSA for HMF electrooxidation, compared to the other catalysts. Further investigation using electrochemical impedance spectroscopy (EIS) (Fig. S11d, ESI†) revealed that Cu–CoO (1 : 3) exhibited the lowest charge transfer resistance, indicating the fastest charge transfer among the catalysts.

Given the hydroxymethyl and aldehyde groups in the HMF molecule, two possible pathways have been established for HMF electrooxidation to FDCA (Fig. S14, ESI†).[27] These pathways lead to different intermediates: Pathway 1 forms the intermediate 5-hydroxymethyl-2-furancarboxylic acid (HMFCA), while pathway 2 produces the intermediate 2,5-diformylfuran (DFF).[28] Both intermediates are further oxidized into 5-formyl-2-furancarboxylic acid (FFCA), which is ultimately converted into FDCA. The reaction pathway is pH-dependent. When pH $\geq$ 13, the –CHO group of HMF preferentially adsorbs onto the catalyst surface, leading to the oxidation of the –CHO group first, which results in the formation of HMFCA (pathway 1).[29]

The electrocatalytic performance of the optimal Cu–CoO (1 : 3) heterostructure nanosheets for HMF conversion was further examined in a 1.0 M KOH electrolyte (10 mM HMF) at 1.45 V. Various applied potentials were utilized in this study (Fig. S15, ESI†). At applied potentials of 1.35 V and 1.40 V, the current response was lower, suggesting reduced efficiency relative to 1.45 V. At the higher potential of 1.50 V, visible oxygen was observed on the electrode. Consequently, the moderate potential of 1.45 V was selected for the electrolysis experiments. The concentration changes of various compounds as a function of the reaction charge were monitored using high-performance liquid chromatography (HPLC). Theoretically, 58C (charge) is required to completely convert HMF (10 mL, 10 mM) to FDCA in the electrolyte. During the electrolysis process with Cu–CoO (1 : 3), as the charge passed increased, there was a reduction in the peak intensity of HMF, along with a corresponding rise in FDCA levels (Fig. 2b). Upon achieving 58C (reaction charge) during chronoamperometric testing (Fig. S16, ESI†), the anode electrolyte changed to colorless, indicating the completion of HMF conversion (Fig. S17, ESI†).

Additionally, HMFCA and FFCA were detected during electrolysis, whereas DFF was not, suggesting that the reaction followed pathway 1. According to the calibration curves for HPLC (Fig. S18, ESI†), the concentrations of the oxidation products for Cu–CoO (1 : 3) were determined and are presented in Fig. 2c. After the reaction, 100% HMF conversion was achieved, resulting in an FDCA yield of 98.2% and a Faradaic efficiency (FE) of 98.1%, outperforming most reported catalysts (Table S1, ESI†). The Cu–CoO catalyst exhibits a two-dimensional structural morphology, which leads to the exposure of a greater number of active sites, thereby enhancing its catalytic performance. Furthermore, the FDCA yield for Cu–CoO (1 : 2) is 63.5%, with an FE of 63.3%. For Cu–CoO (1 : 4), the FDCA yield is 77.6%, with an FE of 77.4% (Fig. S19, ESI†). In comparison, Cu–CoO (1 : 3) exhibits the best catalytic performance. This is consistent with the C_{dl} results, indicating that the increased double-layer capacitance contributes to the enhanced catalytic efficiency by increasing the electrochemical active surface area (Fig. S20, ESI†).

Furthermore, as shown in Fig. 2d, after four consecutive electrolysis cycles, the FDCA yield remained above 95%, and the FE did not significantly decrease, demonstrating excellent cycling durability. The Cu–CoO (1 : 3) catalyst after the reaction was further examined *via* TEM and XPS. The TEM images indicated that the morphology of Cu–CoO (1 : 3) remained almost unchanged (Fig. S21, ESI†). In Fig. S22 (ESI†), the XPS result of Cu–CoO (1 : 3) reveals that Cu converts to CuO during the electrooxidation process, which can inhibit the OER.[8,11–14] After several cycles, the Cu 2p peaks shifted to higher binding energies, while the Co 2p peaks shifted to lower binding energies, indicating an electron interaction between the two substances. This observation suggests that electrons were transferred from Cu to CoO, rendering CoO an electron-rich center and Cu an electron-deficient center.

To understand the enhanced electrocatalytic performance of Cu–CoO in HMF electrooxidation, we performed open-circuit potential (OCP) measurements and density functional theory (DFT) calculations. The OCP measurements revealed variations in the adsorbent within the inner Helmholtz layer, enabling us to estimate the HMF adsorption on the catalyst. As shown in Fig. 3a, the introduced 10 mM HMF to the electrolyte caused a more significant drop in OCP for Cu–CoO (1 : 3) compared to CoO, suggesting stronger HMF adsorption on Cu–CoO (1 : 3).

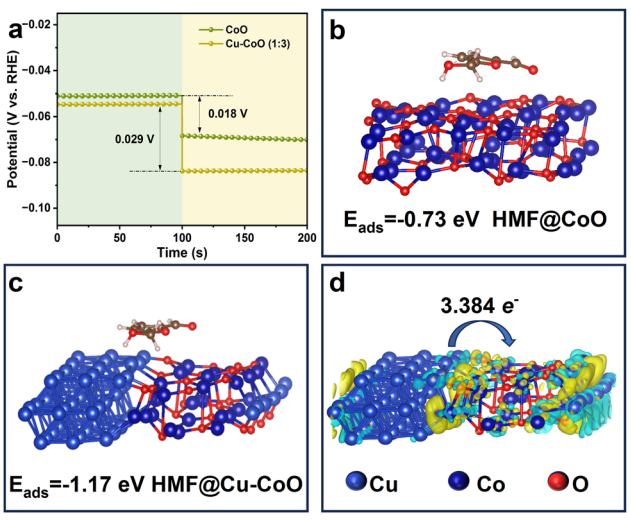

Fig. 3 (a) Open-circuit potential curves of CoO and Cu–CoO (1 : 3) in 1.0 M KOH solution (with or without 10 mM HMF). (b) Adsorption energy of HMF on CoO. (c) Adsorption energy of HMF on Cu–CoO (1 : 3). (d) Charge density difference plots (yellow: charge accumulation; cyan: charge depletion).

For DFT calculations, the structural models of CoO and Cu–CoO were illustrated and optimized (Fig. S23 and S24, ESI†). The HMF adsorption energy on Cu–CoO (1 : 3) was calculated to be −1.17 eV, which is lower than the −0.73 eV observed for CoO (Fig. 3b and c, Table S2, ESI†). This indicates that Cu–CoO (1 : 3) has a stronger adsorption ability for the HMF molecule, consistent with the results from OCP measurement. The lower adsorption energy reduces the reaction barrier, thereby enhancing the HMF electrooxidation on the Cu–CoO (1 : 3) catalyst. In Fig. 3d, the yellow region represents charge accumulation, while the cyan region signifies charge depletion. This result demonstrates that the heterostructure causes electron accumulation at Cu–CoO interface, with electron transfer and redistribution. This electron buildup at the interface accelerates electron transfer and boosts electrocatalytic activity, facilitating the HMF electrooxidation. Moreover, the Bader charge analysis provides further evidence of the electron transfer mechanism, with a charge transfer of 3.384 e^- from Cu to CoO when the heterostructure forms (Table S3, ESI†). This charge redistribution enhances the electronic environment at the catalyst surface, facilitating stronger HMF adsorption and lowering the energy barrier for the electrooxidation reaction. This is consistent with the XPS results. Thus, the DFT calculations highlight the critical role of the Cu–CoO heterostructure in facilitating the electron transfer rate, enhancing HMF adsorption, and optimizing electrocatalytic activity.

In summary, this work successfully designed and developed Cu–CoO heterostructure nanosheets as an efficient electrocatalyst for the electrooxidation of HMF to FDCA. These Cu–CoO nanosheets demonstrated outstanding electrocatalytic performance, achieving 100% HMF conversion, 98.2% FDCA yield, and 98.1% Faraday efficiency. The superior electrocatalytic activity of the Cu–CoO heterostructure arises from its enhanced adsorption capacity for HMF and the facilitated electron transfer at the Cu–CoO interface. DFT calculations further confirmed these findings, underscoring the role of interfacial electron redistribution in improving catalytic efficiency. This study not only provides a high-performance electrocatalyst for biomass conversion but also emphasizes the importance of interfacial engineering in catalyst design.

This work was supported by the National Natural Science Foundation of China (No. 22473070) and Shandong Provincial Natural Science Foundation (No. ZR2024MB146).

Data availability

The data supporting this article have been included as part of the ESI.†

Conflicts of interest

There are no conflicts to declare.

Notes and references

1 Y. Wang, Y. Wang, Y. Lu, Q. Cao and W. Fang, *Chem. Commun.*, 2021, **57**, 1742–1745.
2 L. Hu, L. Lin, Z. Wu, S. Zhou and S. Liu, *Renewable Sustainable Energy Rev.*, 2017, **74**, 230–257.
3 X. Deng, G. Xu, Y. Zhang, L. Wang, J. Zhang, J. Li, X. Fu and J. Luo, *Angew. Chem., Int. Ed.*, 2021, **60**, 20535–20542.
4 S. Sun, Z. Liu, Z. J. Xu and T. Wu, *Appl. Catal., B*, 2024, **358**, 124404.
5 P. Xu, Z. Bao, Y. Zhao, L. Zheng, Z. Lv, X. Shi, H. Wang, X. Fang and H. Zheng, *Adv. Energy Mater.*, 2024, **14**, 2303557.
6 X. Huang, J. Song, M. Hua, Z. Xie, S. Liu, T. Wu, G. Yang and B. Han, *Green Chem.*, 2020, **22**, 843–849.
7 Y. Wu, L. Ma, J. Wu, M. Song, C. Wang and J. Lu, *Adv. Mater.*, 2024, **36**, 2311698.
8 B. J. Taitt, D.-H. Nam and K.-S. Choi, *ACS Catal.*, 2019, **9**, 660–670.
9 W. Wang, H. Xu, T. Sang, D. Ji, J. Hao and Z. Li, *Chem. Commun.*, 2024, **60**, 4214–4217.
10 C. Liu, X. Shi, K. Yue, P. Wang, K. Zhan, X. Wang, B. Y. Xia and Y. Yan, *Adv. Mater.*, 2023, **35**, 2211177.
11 Q. Zhu, B. Gong, S. Huang, Y. Jin, S. Liu, S. Shao, Y. Yang, T. Cataldo, N. M. Bedford and J. C.-H. Lam, *Green Chem.*, 2024, **26**, 4135.
12 J. Chen, H. Yang, H. Fu, H. He, Q. Zeng and X. Li, *Phys. Chem. Chem. Phys.*, 2020, **22**, 11508–11518.
13 Y. Zhang, Z. Xue, X. Zhao, B. Zhang and T. Mu, *Green Chem.*, 2022, **24**, 1721–1731.
14 P. Zhou, X. Lv, S. Tao, J. Wu, H. Wang, X. Wei, T. Wang, B. Zhou, Y. Lu, T. Frauenheim, X. Fu, S. Wang and Y. Zou, *Adv. Mater.*, 2022, **34**, 2204089.
15 D.-H. Nam, B. J. Taitt and K.-S. Choi, *ACS Catal.*, 2018, **8**, 1197–1206.
16 C. Li, F. Wang, Y. Nie, L. Wang, Z. Zhang, T. Liu, B. He, Y. Ma and L. Zang, *Chem. Eng. J.*, 2024, **481**, 148580.
17 Y. Jia, Z. Gui, W. Zhang, T. Yan, J. Tan, L. Chen, Q. Gao, Y. Zhang and Y. Tang, *ACS Appl. Mater. Interfaces*, 2024, **16**, 8697–8706.
18 G. Yang, Y. Jiao, H. Yan, Y. Xie, A. Wu, X. Dong, D. Guo, C. Tian and H. Fu, *Adv. Mater.*, 2020, **32**, 2000455.
19 L. Yang, R. Liu and L. Jiao, *Adv. Funct. Mater.*, 2020, **30**, 1909618.
20 W. Jia, B. Liu, R. Gong, X. Bian, S. Du, S. Ma, Z. Song, Z. Ren and Z. Chen, *Small*, 2023, **19**, 2302025.
21 G. Yang, Y. Jiao, H. Yan, Y. Xie, A. Wu, X. Dong, D. Guo, C. Tian and H. Fu, *Adv. Mater.*, 2020, **32**, 2000455.
22 P. Jin, L. Zhang, Z. Wu, B. Zhou, Z. Duan, H. Li, H. Liu, A. Deng, Q. Li, Y. Zhang, C. Zhao and S. Wang, *Chem. Eng. J.*, 2024, **481**, 148303.
23 L. Pang, A. Barras, Y. Zhang, M. A. Amin, A. Addad, S. Szunerits and R. Boukherroub, *ACS Appl. Mater. Interfaces*, 2019, **11**, 31889–31898.
24 Q. Zhou, R. Sun, Y. Ren, R. Tian, J. Yang, H. Pang, K. Huang, X. Tian, L. Xu and Y. Tang, *Carbon Energy*, 2023, **5**, e273.
25 Y. Zhao, T. Xu, X. Bai, Y. Jia, Y. Pan, X. Shi, H. Zheng and L. Zheng, *Chem. Eng. J.*, 2024, **482**, 149054.
26 H. Wu, X. Chen, H. Xu, R. Yang, X. Wang, J. Chen, Z. Xie, L. Wu and Y. Mai, *Nano Res.*, 2024, **17**, 7991–7999.
27 J. Liu and S. Tao, *Adv. Sci.*, 2023, **10**, 2302641.
28 N. Shang, W. Li, Q. Wu, H. Li, H. Wang, C. Wang and G. Bai, *J. Colloid Interface Sci.*, 2024, **659**, 621–628.
29 Y. Yang and T. Mu, *Green Chem.*, 2021, **23**, 4228.

